3D electrical imaging of the inner structure of a complex lava dome, Puy de Dôme volcano (French Massif Central, France)

Angélie Portal, Y. Fargier, P. Labazuy, J.-F. Lénat, P. Boivin, D. Miallier

3D electrical imaging of the inner structure of a complex lava dome, Puy de Dôme volcano (French Massif Central, France)

A. Portal[1,4*], Y. Fargier[2], P. Labazuy[1], J.-F. Lénat[1], P. Boivin[1], D. Miallier[3]

[1] {Université Clermont Auvergne, CNRS, IRD, OPGC, LMV, F-63000 Clermont-Ferrand, France}

[2] {GERS, IFSTTAR, Bron, France}

[3] {Université Clermont Auvergne, CNRS–IN2P3, LPC, F-63000 Clermont-Ferrand, France}

[4] {BRGM, DRP/IGT, 3 avenue Claude Guillemin, BP 36009, 45060 Orléans, France}

* Corresponding author at: BRGM, 3 avenue Claude Guillemin, 45060 Orléans Cedex 2, France.
Tel.: +33 (0) 2 38 64 32 34
E-mail address: a.portal@brgm.fr

Key words: Lava dome; Electrical Resistivity Tomography; 3D inversion; Puy de Dôme volcano

Abstract

Lava domes result from extrusion of massive lava, frequent explosions and collapses. This contribution focuses on a complex trachytic lava dome, the Puy de Dôme volcano, located in the Chaîne des Puys volcanic field (French Massif Central, France). We performed Electrical Resistivity Tomography (ERT) acquisitions on the entire edifice in order to investigate its overall inner structure as well as to detail its summit area. The resulting large ERT dataset integrated a recently developed 3D inversion code based on an unstructured discretization of the geometrical model. The 3D inversion models obtained refine the existing geological model of the Puy de Dôme's inner structure obtained by previous geophysical studies. These results also highlight the strong fracturing and fumarolic alteration that affect the summit part of the volcano.

1. Introduction

Volcanic lava domes are complex structures built up by highly viscous magmas and formed by both intrusion and extrusion processes. During their growth, gravitational instabilities create talus formed by rockfalls, and large collapses may

trigger explosive eruptions (*e.g.* Mount St Helens 1980, Christiansen and Peterson, 1981; Soufrière Hills, Herd et al., 2005) and pyroclastic flows (*e.g.* Unzen volcano 1991, Sato et al., 1992). Because their construction is often incremental and/or polyphase, lava domes are usually compound edifices. Even in the case of composite lava domes whose construction has been monitored, their inner structure remains difficult to establish because of the intercalation of massive lava, talus breccia and pyroclastites, and also because endogenous processes, such as magma intrusion or hydrothermal activity, cannot be observed at the surface. Nevertheless, an understanding of volcanic dome construction and evolution is an important issue for hazard assessment.

Here, we have used the Electrical Resistivity Tomography – ERT - method to study the internal structure of a large Holocene lava dome, the Puy de Dôme, in the French Massif Central. The ERT technique, initially developed for environmental investigations and engineering (Chambers et al., 2006; e.g. Dahlin, 1996; Loke et al., 2013 and references therein), is now widely used in volcanology (e.g. Barde-Cabusson et al., 2014; Brothelande et al., 2015; Byrdina et al., 2018; Fikos et al., 2012; Gresse et al., 2017; Soueid Ahmed et al., 2018). As a large range of resistivity values is expected in lava domes, this imaging technique is well suited to the study of their inner structure, as shown by the example of La Soufrière de Guadeloupe lava dome (Brothelande et al., 2014; Lesparre et al., 2014; Nicollin et al., 2006).

This study presents the main results from ERT surveys performed on the Puy de Dôme volcano between 2011 and 2014. Given the spatial geometry of the datasets, we were able to carry out a 3D inversion approach, in order to better constrain the inner structure of the volcano. For this purpose, we used a recent inversion code developed by Fargier et al. (2017). Our inversion strategy was first to study the whole lava dome, and then to focus on its summit area only. The geological interpretation of the 3D inversion models provides new information about the dome's inner structure. We propose a comparison between electrical resistivity models and results obtained from gravity and magnetic measurements (Portal et al., 2016) and discuss the synthetic geological model of the Puy de Dôme volcano.

2. Geological and structural settings

The Puy de Dôme volcano is located in the Chaîne des Puys volcanic field, the most recent manifestation of the French Massif Central volcanism, composed of

around 80 aligned Quaternary monogenetic volcanoes (scoria cones, lava domes and maars) (Boivin et al., 2017). The Puy de Dôme, an 11,000 years old trachytic lava dome, is the largest edifice of the volcanic chain with an elevation of 1465 m, a basal diameter between 1.5 and 2 km and an apparent height of 400 m (**Fig. 1**). The dome is emplaced into a cluster of several scoria cones and their associated lava flows (Boivin et al., 2017; Miallier et al., 2010; Portal et al., 2016). Geological studies, based on field observations, initially propose a three-stage construction model for the Puy de Dôme growth (Camus, 1975): 1) the growth of a first cumulo-dome, 2) the partial destruction of its eastern part and 3) the growth of a second lava spine into the resulting collapse scar. Recent works modify this model and suggest that the eastern flank would result from a change in the eruptive dynamism and not from a flank collapse (Boivin et al., 2017). Miallier et al. (2010) propose that the dome eruption ended with a final explosive activity interpreted as a summit phreatic/phreatomagmatic eruption. The rock alteration on several outcrops in the summit area prove that a strong hydrothermal activity accompanied the Puy de Dôme growth. Debris and/or pyroclastic flows also occurred as shown by the fans of unconsolidated materials observed at the base of the volcano (Portal et al., 2016). Finally, Boudon et al. (2015) suggest that the hydrothermal activity progressively led to a silicified permeable lava dome through cristobalite deposition into the pores and deep-seated fractures.

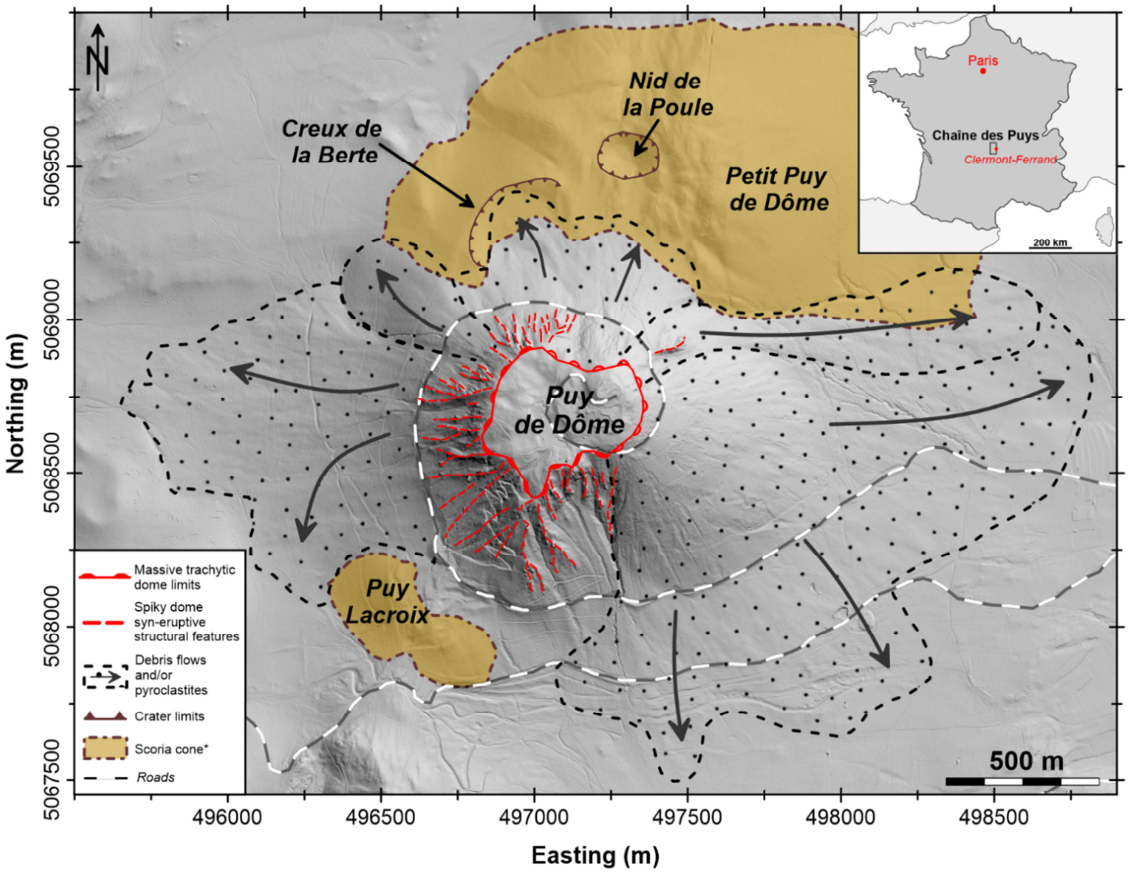

Fig. 1. Simplified map of the main morphological features observed on the Puy de Dôme volcano and its surrounding after the analysis of the high resolution DTM by Portal et al. (2016). The scoria cones limits are identified from Boivin et al. (2017). Coordinates: WGS84 – UTM31N.

The geological interpretation of the recent geophysical results (gravity and magnetism) obtained by Portal et al. (2016) suggests that:

1. The upper part of the lava dome could be constituted of a carapace of solid rocks, that is morphologically well-defined in the western part (**Fig. 1**);
2. The eastern flank of the volcanic dome, very regular from the top to the base could be buttressed, in its summit part, by an underlying massive carapace of rocks or welded pyroclastites;
3. The central part of the dome might be composed of successive massive intrusions and extrusions of trachyte interbedded with collapse breccia.

3. ERT measurements

3.1. Data acquisition

We performed twelve ERT profiles of different lengths on the Puy de Dôme

volcano, between 2011 and 2014 (**Table 1**). The goal was to investigate the geological structures at different scales (the entire edifice on the one hand and its summit area on the second hand). We defined a unique central point at the top of the volcano through which we connected all the profiles crossing the area. We used a multi-electrode ABEM system (Terrameter SAS 4000) associated with an electrode selector (ES10-64) for data acquisitions. A standard ERT configuration was composed of 64 stainless steel electrodes. To improve ground/electrode contact we used clay and salty water. We applied the Wenner-alpha and Wenner-Schlumberger protocols due to their good signal-to-noise ratio, their optimal depth of investigation and their sensitivity to horizontal and vertical geological contrasts (Dahlin et Zhou, 2004). We acquired every measurement at least three times, in order to calculate a standard deviation on the data. A standard deviation value greater than 5% (threshold fixed by the operator) led to additional measurements (up to 4 stacks).

ERT lines were first deployed at the scale of whole dome (**Fig. 2a**). Two perpendicular profiles allowed us to explore its inner structure (**Table 1**): an approximately N-S 35 m electrode-spacing line (P1, 2.2 km-long) and a W-E line (P2-1, 2.2 km-long), the latter performed in two stages. Indeed, an equipment problem affected the measurements along the eastern part of the initial P2-1 profile (beyond the 32th electrode). This led to data with very low signal-to-noise ratio that we eliminated. To complete the truncated P2-1 dataset, we deployed a new line from the summit to the volcano's eastern base (P2-2, 64 electrodes, 10 m electrode spacing). We performed this 1.3 km-long line using two half-length roll-along. This strategy results in a depth of investigation greater in the western part than in the eastern one. Last, we performed two supplementary profiles on the southern flank (P3) and at the eastern base (P4) of the volcano (**Fig. 2** and **Table 1**).

	Name	Date	Number of electrodes	Electrode spacing (m)	Coordinates (m, WGS84 - UTM31N)			
					Start electrode		End electrode	
					X	Y	X	Y
Whole dome	P1	06/2011	64	35	497466.54	5069700.19	496750.96	5067823.45
	P2-1	06/2013	32	35	496175.36	5069129.13	497075.61	5068754.54
	P2-2*	04/2014	128	10	497094.13	5068743.52	498169.52	5068440.54
	P3	04/2014	64	10	497094.77	5068739.40	497254.84	5068236.55
	P4	04/2014	64	10	497804.31	5068989.46	498043.67	5068428.31
Summit area	P5*	06/2011	128	5	497177.05	5069013.00	496953.86	5068473.31
	P6*	06/2011	128	5	496839.90	5068887.82	497380.95	5068691.14
	P7•	01/2014	51	10	496962.63	5068997.07	497183.99	5068589.63
	P8•	01/2014	64	5	497018.52	5068873.90	497173.54	5068606.14
	P9°	04/2014	64	10	496855.39	5068562.44	497325.74	5068919.28
	P10°	01/2014	64	5	496974.28	5068649.88	497214.65	5068845.12
	P11	04/2014	64	5	497054.46	5068936.99	496939.20	5068652.20

*: roll-along acquisitions ; • and °: overlapped profiles

Table 1. Characteristics of the ERT profiles performed on the Puy de Dôme volcano, with variable electrode spacing.

We also carried out a detailed study of the summit area using profiles with electrode spacing of 5 m (P5, P6, P8, P10 and P11) and 10 m (P7 and P9) (**Table 1**). All the profiles intersecting at the same location as the long lines (**Fig. 2b**). Half-length roll-along processes allowed us to extend two 5 m electrode spacing lines, P5 and P6. We could not expanded the P7 line beyond the 51th electrode because of the presence of an access road and a railway.

We obtained the electrodes locations through differential GPS measurements (GPS Topcon) with post-treatment of the data using the Topcon Tools software (leading to centimetric precision in planimetry and altimetry). In some sectors, under tree cover, we have extracted electrode elevation from the 0.5 m resolution DTM.

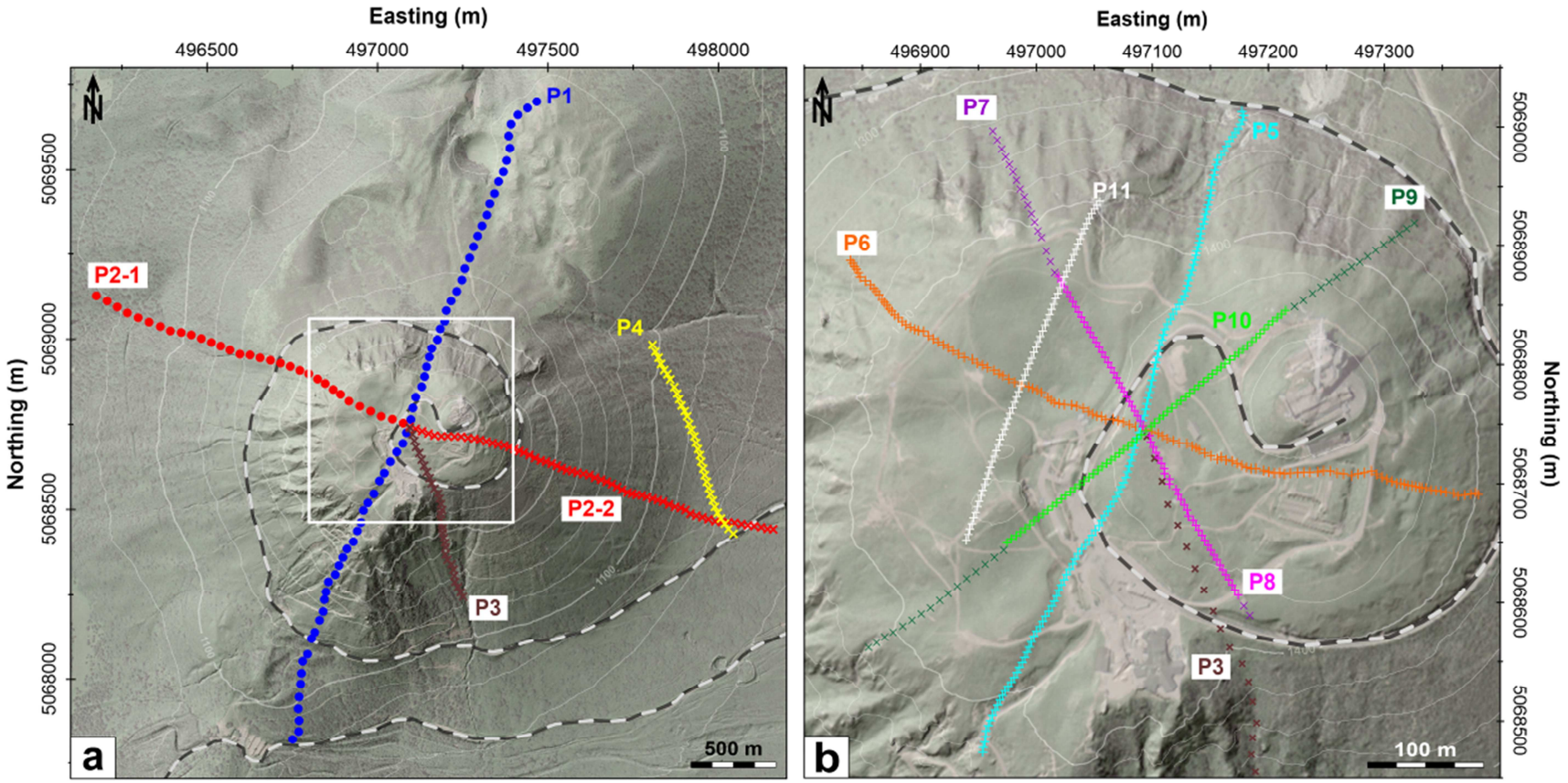

Fig. 2. (a) Location of the ERT profiles on the whole Puy de Dôme volcano. (b) Location of the ERT lines on the summit area. For P3 and P4 (a) we represent one electrode out of two. Coordinates: WGS84 – UTM31N.

3.2. Data processing and inversion

The reliability of the electrical resistivity distribution obtained from inversion models significantly depends on the data quality. Efforts were made during field measurements to lower data noise as much as possible by ensuring both good electrode/ground contacts and setting robust acquisition parameters. Several resistivity measurements were stacked and the resulting standard deviation q (also called quality factor) is less than 1% for most of the datasets. Raw resistivity data were filtered through a quality-based method (Brothelande et al., 2014), to eliminate data characterized by a low signal to noise ratio. All the measurements with an electrical potential difference of less than 1 mV and/or error higher than 5% were rejected. Before inversion, we used X2IPI software (Robain and Bobachev, 2017) to filter all datasets in order to remove artifacts due to the presence of strong heterogeneities in the shallow levels of the measurements. Finally, visualization of the data in pseudo-sections allowed us to eliminate the remaining spurious measurements.

To perform the 3D inversion of our resistivity data, we use an inversion code developed by Fargier et al. (2017). This algorithm is based on a conventional Gauss-Newton smoothness-constrained method with an Occam-type regularization (Constable et al., 1987; de Groot-Hedlin et Constable, 1990; Lines et Treitel, 1984). It also uses a non-structured discretization method (tetrahedral mesh, **Fig. 3**; Rücker et al., 2006), that is now widespread for inversion of ERT datasets, especially in volcanology (e.g. Gresse et al., 2017; Revil et al., 2010; Rosas-Carbajal et al., 2016; Soueid Ahmed et al., 2018). A complete description of this inversion code is given by Fargier et al. (2017). The RMS (Root Mean Square) error, representing the difference between the model response and the measured data, quantifies the reliability of the inversion models.

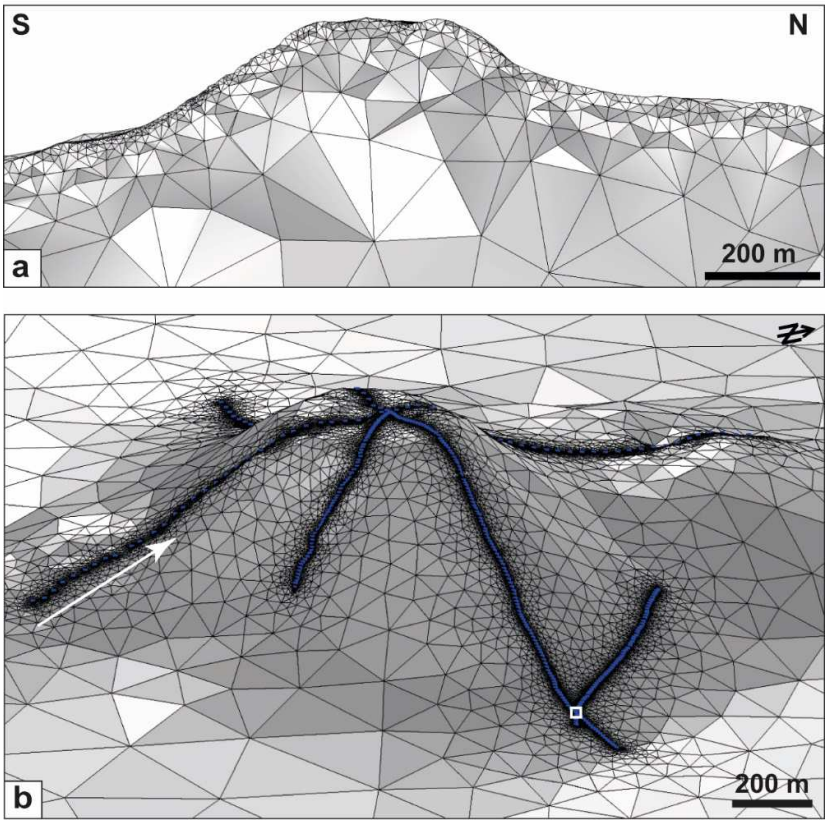

Fig. 3. (a) Vertical section in the 3D mesh along the P1, north-south oriented profile (location of this section is indicated by the white arrow on b). (b) 3D surface mesh with topography of the Puy de Dôme volcano, the blue dots represent the location of the electrodes.

We divide the total data set (6709 measurements) in two to perform the 3D inversion. The two derived datasets rely on the repartition and the geometry of the acquisition profiles as well as on our knowledge on the complexity of the geological structure of the dome. Thus, the first inversion named WDI (Whole Dome Inversion), integrates the ERT profiles P1 to P4 (**Table 1** and **Fig. 2a**). It aims to constrain the overall structure of the entire edifice in order to highlight the main structures inside the lava dome. The second inversion SAI (Summit Area Inversion) focuses on the summit lines P5 to P11, (**Table 1** and **Fig. 2b**) to detail the summit part of the volcano. For each inversion set, we fix a homogeneous initial model for the first iteration with a resistivity equal to the mean resistivity of the input dataset. Each following iteration uses the model of the previous one as reference. Our approach to treat the data independently (two distinct initial model) lies on the ambition to limit the propagation of error from the first model to the other.

4. Results

The inversion model of the whole Puy de Dôme (WDI) is associated to a global RMS error of 7.8%. We extract horizontal sections (**Fig. 4**) and vertical ones (**Fig. 7**, **Fig. 8a** and **Fig. 9a**) in the 3D model. The global RMS error of the detailed 3D inversion model of the summit area (SAI) is 12.7%. Horizontal (**Fig. 5**) and vertical **(Fig. 6**) sections of this model have been extracted for description.

The presence of many man-made structures (roads, rails, paths…) affects the inversion models. We identified resulting artifacts (highly conductive patches, red triangles on **Fig. 6** to **Fig. 9**) that will not take part of the following description/interpretation. Human activity has also strongly reworked the summit area of the Puy de Dôme, as evidenced by archeological vestiges and buildings. This support our choice to not describe and interpret any resistivity anomaly in the first ten meters of the SAI models (**Fig. 6**). Although the inversion integrates the loss of information and constraints between profiles and with depth by an increase of both the tetrahedrons size (Fig. 3) and the smoothing factor, we delineate opacity masks on horizontal (**Fig. 4** and **Fig. 5**) and vertical sections (**Fig. 6** and **Fig. 7**). We delineate a buffer area along the profiles for the horizontal sections (the buffer distance equal to twice the electrode spacing). For the vertical sections, we used the data distribution with depth taking into account the topography. The objective of the masks is to focus the description and interpretation of the models in the better constrained areas.

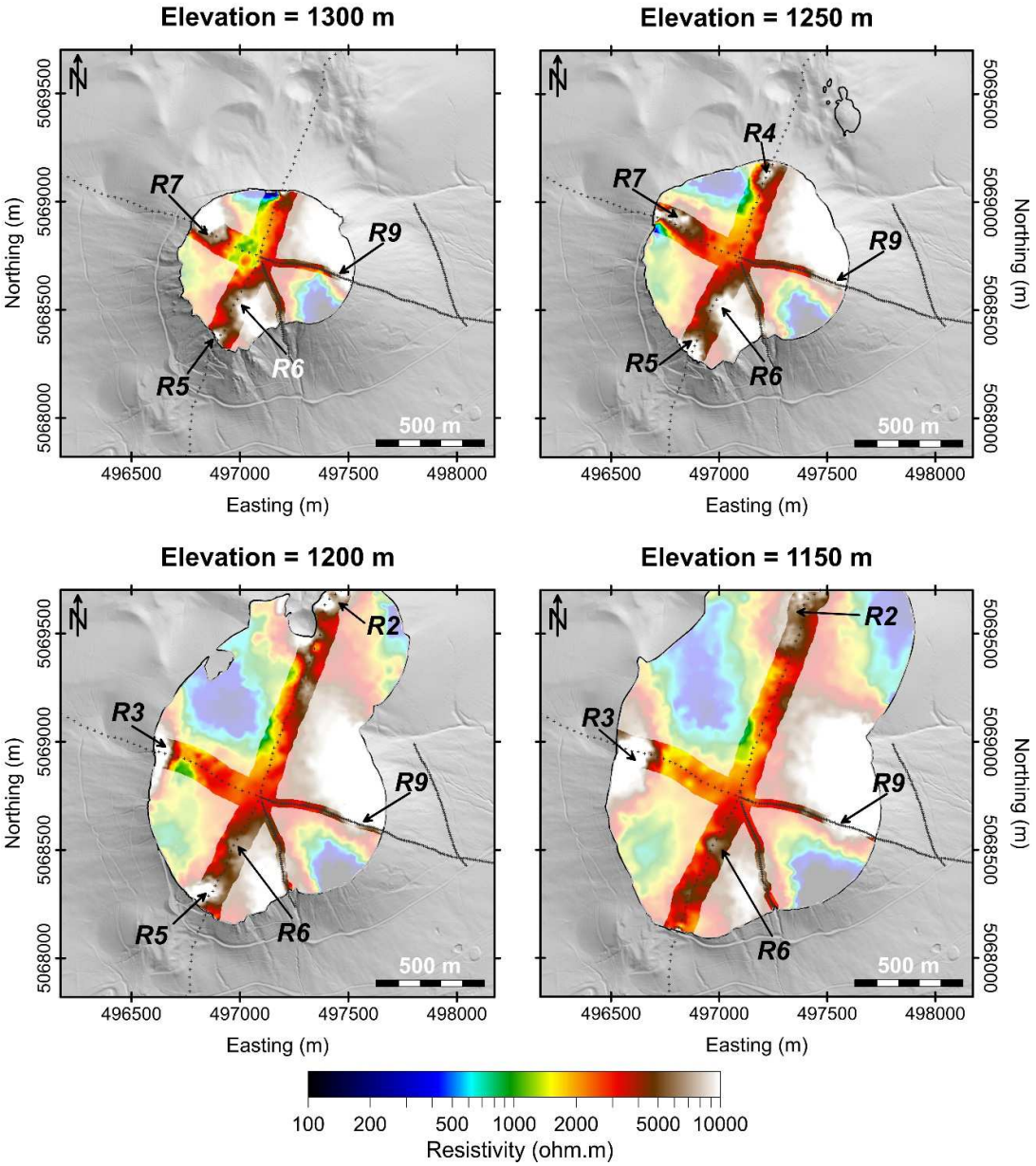

Fig. 4. Horizontal sections of the 3D inversion model of the Puy de Dôme (WDI). Sections every 50 m, starting from the elevation of 1300 m (top left) to 1150 m (bottom right). Black dots indicate the position of the electrodes. Opaque zones delineate the areas less constrained by ERT measurements. Coordinates: WGS84 – UTM31N.

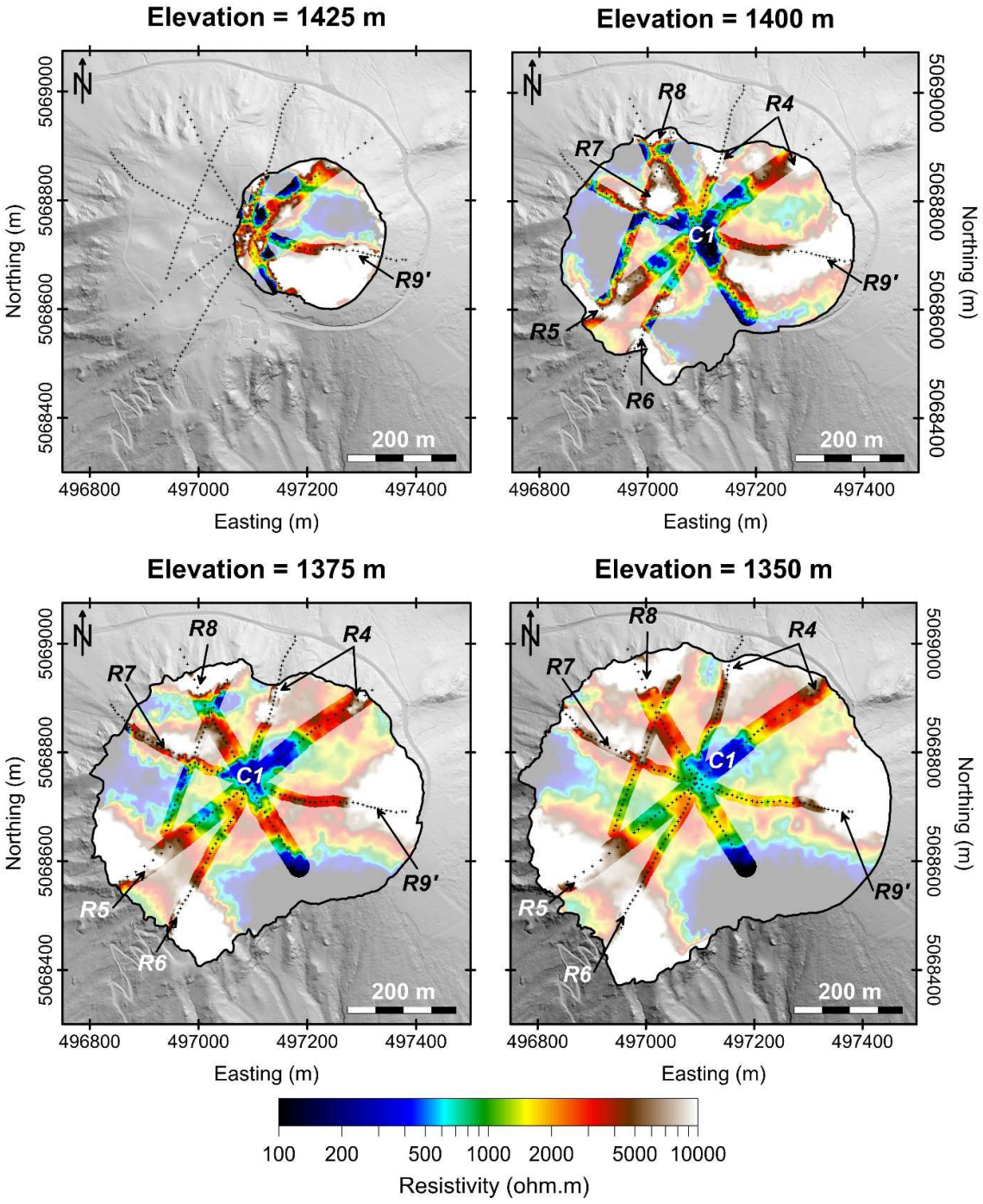

Fig. 5. Horizontal sections of the 3D inversion model of the summit area of the Puy de Dôme (SAI). Sections every 25 m, starting from the elevation of 1425 m (top left) to 1350 m (bottom right). Black dots indicate the position of the electrodes. Opaque masks delineate the areas less constrained by the ERT measurements. Coordinates: WGS84 – UTM31N.

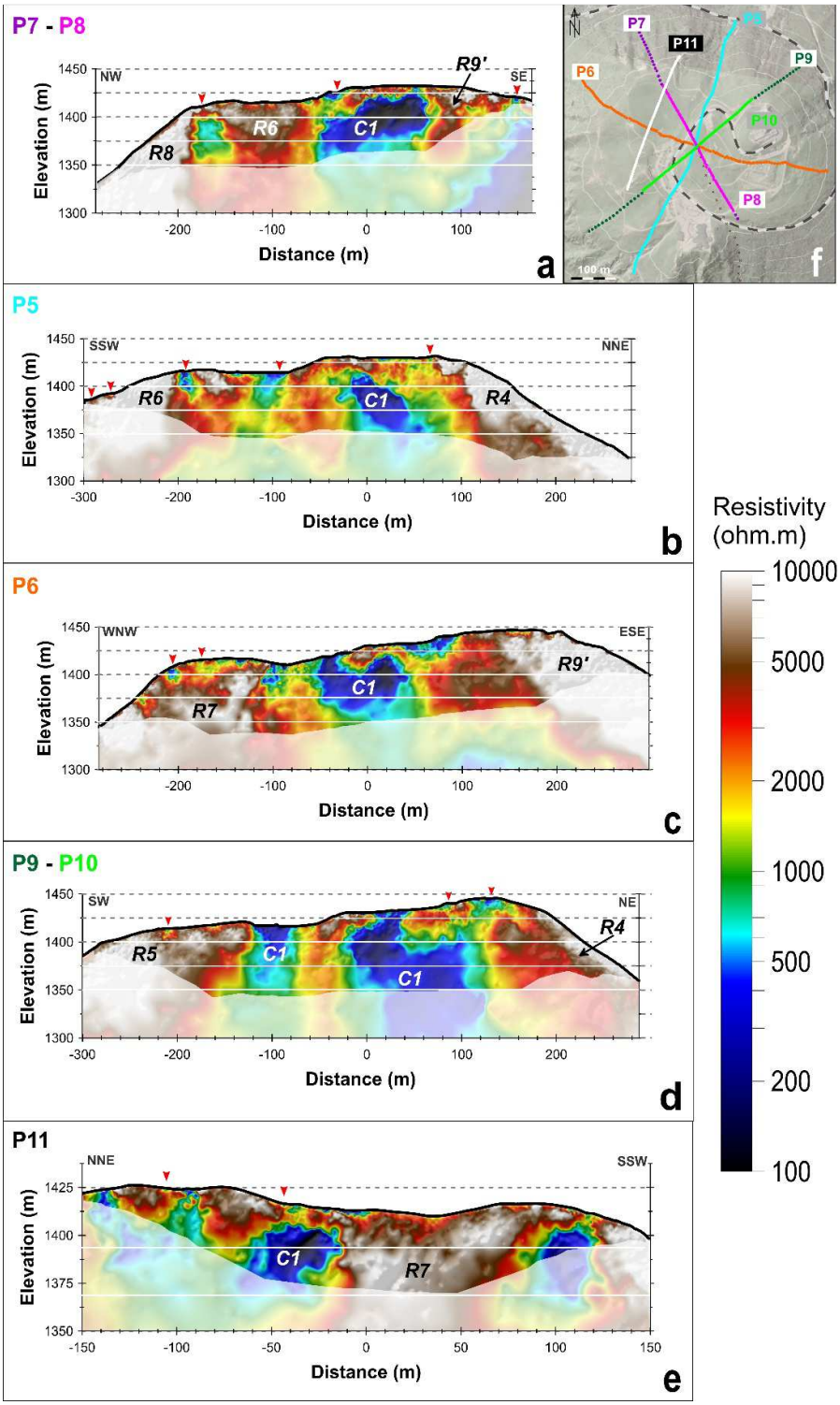

Fig. 6. Vertical sections extracted from the 3D inversion model of the summit area of the Puy de Dôme volcano (SAI): (a) P7-P8, (b) P5, (c) P6, (d) P9-P10, (e) P11. (f) Map of the location of the ERT lines. Opaque masks delineate the areas less constrained by the ERT measurements. Red triangles indicate local conductive patches associated to man-made structures (roads, paths, rail…). White lines refers to horizontal slices on **Fig. 5**. Rn and Cn represent specific features related to resistive and conductive bodies, respectively.

196 There is a wide range of resistivity variations at the scale of the Puy de Dôme,
197 from conductive values (ρ~100 Ohm.m) to resistive ones (ρ~10 kOhm.m). The mean
198 resistivity of the dome is about 2000-3000 Ohm.m.

199 We identify several highly resistive structures (ρ>5000 Ohm.m):

200 - The *R1* and *R2* bodies are present near the model edges (**Fig. 4** and
201 **Fig. 8a**);

202 - A large highly resistive (ρ>9000 Ohm.m) body, *R3*, is identified in the lower
203 part of the western flank (**Fig. 4** and **Fig. 9a**). This structure is visible around
204 an elevation of 1250 m and could extend beyond the maximum depth of
205 investigation;

206 - To the North, a thin and superficial (around 30 m thick, **Fig. 4** and **Fig. 8a**)
207 *R4* structure follows the slope of the volcano;

208 - To the South, we observe two larger highly resistive bodies. The first one,
209 *R5*, seems to be restricted to the flank (maximum thickness of 120 m). The
210 second, *R6*, reaches the surface (**Fig. 5** and **Fig. 6**) and extends inside the
211 volcano (**Fig. 7a** and **Fig. 8a**). Between an elevation 1200 m and the
212 surface, those two units progressively connect (**Fig. 4** and **Fig. 5**).

213 - A well-delimited resistive structure (*R7*) occupies the upper part of the
214 western flank of the lava dome (**Fig. 4**, **Fig. 5**, **Fig. 6** and **Fig. 9a**). Another
215 resistive structure body, *R8*, develops along the upper part of the NW flank
216 (**Fig. 5** and **Fig. 6**).

217 - Last, we highlight a very large resistive structure along and within the
218 eastern flank. We can distinguish three sub-units. The large and deep *R9*
219 (**Fig. 4** and **Fig. 8b**) structure may extends beyond the maximum depth of
220 investigation (depth>235 m in the central part of this body). In the summit
221 area, the surface *R9'* body is around 30 m thick (**Fig. 6a**) as well as the *R9"*
222 structure at the bottom of the edifice (**Fig. 7b**).

223 A low-resistivity pattern, *C1* (ρ<1000 Ohm.m), is observed in the upper part of
224 the dome, beneath the summit area (**Fig. 7a, Fig. 8a** and **Fig. 9a**). The horizontal
225 slices of the detailed SAI model (**Fig. 5**) show that several highly resistive bodies
226 intersect this *C1* structure.

The detailed summit 3D model (**Fig. 5** and **Fig. 6**) maps more accurately the main resistant structures identified on the entire dome (*R4*, *R5*, *R6, R7, R8* and *R9'*). The *R7* resistive structure extends to the center part of the dome (**Fig. 6c**) and shows an elongated shape in the W-E direction (**Fig. 5**). The *R9'* unit also presents an elongated shape (at an elevation of 1400 m, **Fig. 5**) from the dome's center toward the East.

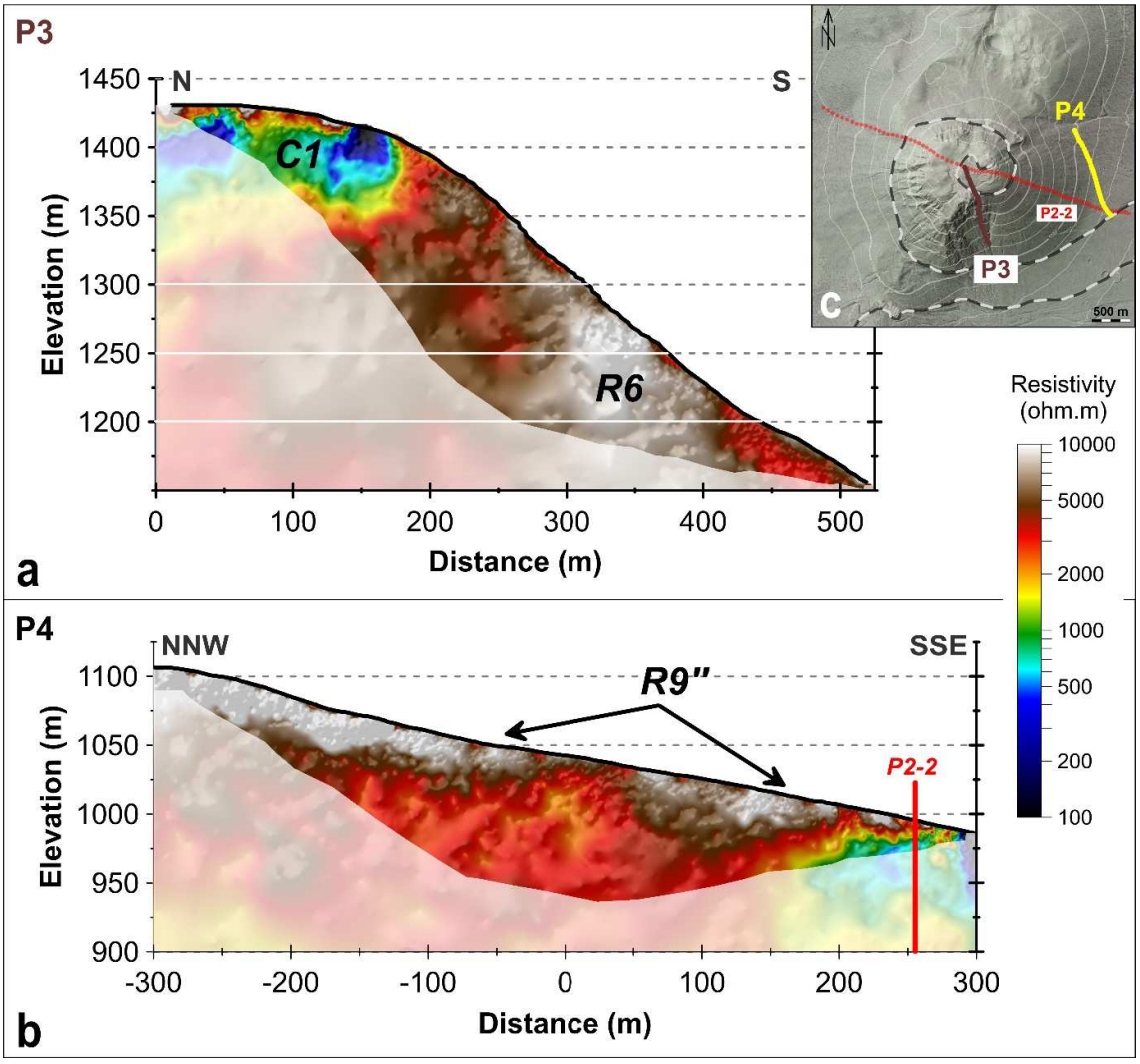

Fig. 7. Vertical sections extracted from the 3D inversion models of the entire Puy de Dôme edifice (WDI). (a) P3 profile. (b) P4 profile. (c) Map of the location of the two ERT lines. Opaque masks delineate the areas less constrained by the ERT measurements. White lines (a) refers to horizontal slices on **Fig. 4**. Rn and Cn represent specific features related to resistive and conductive bodies, respectively.

5. Interpretation and discussion

We base the following interpretation on the resistivity models described above, while comparing them to those of the previous geophysical results (gravity and magnetism, Portal et al., 2016). We first focus on the volcanic formations identified below the Puy de Dôme volcano. Then, we discuss the overall structure of the lava dome before concentrating on the summit part of the Puy de Dôme.

5.1. The surrounding volcanic structures

Within the flanks, we identify high resistivity zones (ρ>5000 Ohm.m). According to morphological analysis (**Fig. 1**), field observations (presence of red scoriae and massive bombs) and previous geophysical results (low density body - 1.6, **Fig. 8b** and **Fig. 9b**; Portal et al., 2016), we can unambiguously interpret *R1* and *R2* as underlying scoria cones (the Puy Lacroix and the Petit Puy de Dôme respectively). The *R3* resistive anomaly, identified on the western flank, also coincides with a low-density body (1.4, Portal et al., 2016). Electric and gravity results confirm the observations made by Miallier et al. (2010) who identify a buried cinder cone in this area, named Cône de Cornebœufs. Our results support and confirm the theory that the Puy de Dôme has grown on top of an area previously occupied by a swarm of cinder cones (Boivin et al., 2017; Portal et al., 2016).

We observe that the dimensions of the *R1* to *R3* anomalies are more limited than the dimensions of the low-density structures identified by Portal et al. (2016) (**Fig. 8** and **Fig. 9**). That lets us suppose a resistivity gradient inside the low-density structures, from the surface toward the lava dome's core. Considering the decrease of the model resolution at depth, we can also hypothesize about a geological origin of this resistivity evolution. This could correspond to an alteration of the existing scoria cones by hydrothermal fluids during the lava dome's growth. Indeed, summit outcrops show evidences of a former fumarolic activity (ochre alteration of the trachyte). The resistivity gradient could also reflect the variation of the water content in the porous scoria formations (piezometric level). However, complementary data are necessary to constrain the numerical and/or the geological contribution of the resistivity gradient identified in the low-density structures.

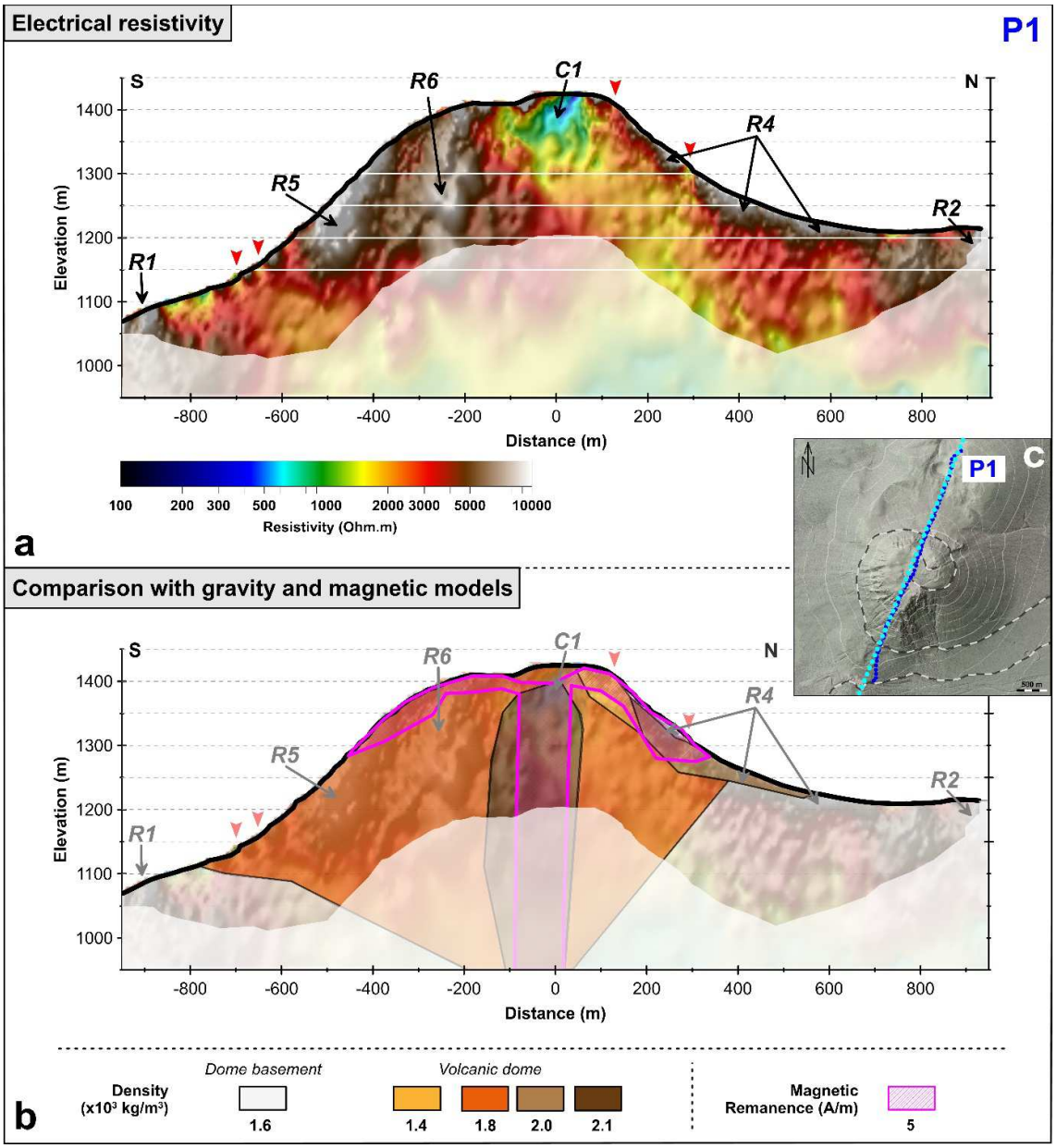

Fig. 8. (a) Vertical section extracted from the 3D inversion models of the entire Puy de Dôme edifice (Whole Dome Inversion – WDI) along the P1 ERT profile. (b) Comparison of the electrical results to the corresponding gravity and magnetic ones from (Portal et al., 2016). (c) Map of the location of the P1 line (blue) and the corresponding section extracted from gravity and magnetism results (cyan dotted line). Opaque masks delineate the areas less constrained by the ERT measurements. Red arrows indicate local conductive patches associated to man-made structures (roads, paths, rails…). White lines (a only) refer to horizontal slices on **Fig. 4**. Rn and Cn represent specific features related to resistive and conductive bodies, respectively.

5.2. New constrains on the overall geological structure of the lava dome

Overall, the resistivity structure of the Puy de Dôme itself highlights several main features: (1) very high resistivity surface or shallow layers on the summit and flanks, (2) an overall resistive interior and base of the edifice, and (3) a low-resistivity zone in the upper part of the dome, beneath the summit area.

The high resistivity units *R4* (its upper part, above and elevation of 1350 m, **Fig. 6b**), *R5, R6*, *R7, R8* (resistivity >5000 Ohm.m, **Fig. 4**, **Fig. 6**, **Fig. 8a** and **Fig. 9a**) coincide with steeply sloping areas. Morphologically, these zones correspond to surface massive trachyte ridges (**Fig. 1**), suspected to extend at shallow depth. The mentioned resistive patterns correspond to low density structures (1.4 to 1.6; Portal et al., 2016). The upper part of *R4* and the *R6* body also show a remanent magnetization of about ~ 5 A/m (**Fig. 9b**). We suggest that these resistive formations are composed of massive trachytic lava bodies. They could be former lava intrusions emplaced during the construction of the spiny dome. At the scale of the entire edifice, the electrical results do not highlight the presence of a massive trachytic carapace as initially proposed by Portal et al. (2016).

The northern flank is globally less resistant (**Fig. 8a**) with no specific density or magnetic signature (**Fig. 8b**). It also present a surface morphology smoother than that of the southern and eastern flanks (**Fig. 1**). These observations suggest that the northern flank would be composed of slightly different material probably with very few or no massive lava and possibly more talus breccia. Below the elevation of 1350 m, the shallow resistive pattern *R4* (ρ>5000 Ohm.m) seems to be associated to an intermediate density – 2.0 - structure and partially magnetized body (5 A/m, **Fig. 8b,** Portal et al., 2016). This resistive formation would correspond to recent pyroclastic density current deposit (Boivin et al., 2017; Portal et al., 2016). Boivin et al. (2017) also describe the presence of tephra-fall deposits in this area, issued from the Kilian's crater eruption, and that could contribute the R4 resistive response.

Our results show that the eastern flank, whose morphology is singular (**Fig. 1**), has a specific and complex high resistivity signature. Indeed, we identify the thick layer *R9*, between 350 m and 850 m of distance along the profile (**Fig. 9a**) and the thinner *R9'* (**Fig. 6c** and **Fig. 9a**) and *R9"* (**Fig. 7b**) bodies. In morphology, the eastern flank looks like a nearly perfect half cone with a mean slope of about 33-35°

(Boivin et al., 2017; Portal et al., 2016). Such a value is too high for a repose angle of loose material (for comparison, the nearby cinder cones have average slopes of less than 25°). Boivin et al. (2017) propose that this eastern flank is mostly composed of consolidated cinder deposits originating from a second exogenous eruptive phase of the dome's construction. According to this hypothesis we suggest that the *R9', R9"* and the surface part of the *R9* (first 30 m) correspond to this welded cinder pyroclastite deposits. Following this eruptive scheme, the high slopes of the eastern flank could be due to an immediate induration process of the cinder products (the mechanisms of such a phenomenon are still under investigation, Boivin et al., 2017). The rest of the *R9* signature (below 30 m from the surface) could correspond to unaltered breccia with massive lava intrusion contemporaneous to the cumulo-dome construction. The lack of morphological evidences of spiky dome features along the eastern flank could result from the pyroclastite emplacement that fill and cover the trachyte ridges. Finally, deep inside the eastern flank of the dome, the density model also suggests a low-density signature (**Fig. 9b**) interpreted as strombolian deposits (Portal et al., 2016). The high resistivity observed in this area (lower part of *R9*, **Fig. 9a**) support this interpretation without giving discriminating criterion.

The rest of the dome's inside has globally relatively high resistivity values (from about 2000 Ohm.m up to 5 000 Ohm.m). Portal et al. (2016) show that these parts of the dome have a generally low density (around 1.8, **Fig. 8b** and **Fig. 9b**) except the presence of a dense (2.1) and magnetized (5 A/m) core. Although the model is less constrained at depth, it seems that the high resistivity values observed inside the lava dome support their interpretation: a conduit composed mainly of massive, poorly fractured and/or altered rocks surrounded by a cogenetic breccia. The corresponding high resistivity values identified suggests that the breccia probably contains former massive intrusions. While the resistivity signature does not allow differentiating both the breccia (low density) and the conduit (high density and magnetization), the latter seems characterized by resistivity values globally slightly lower than the containing formations. The hypothesis proposed here is that, along the conduit, the resistivity signature may result from rock alteration due to fluid circulations during the dome growth and evolution.

Finally, the central upper part area of the dome is very different from the flanks. The sections in **Fig. 8a** and **Fig. 9a** clearly show that this zone is the most conductive

part of the edifice (*C1*, 100-1500 Ohm.m). On the long ERT profiles (P1 and P2), the outlines of *C1* are well highlighted. However, it is with the detailed summit ERT profiles that the complex geometry and organization of this zone can be deciphered (**Fig. 6**).

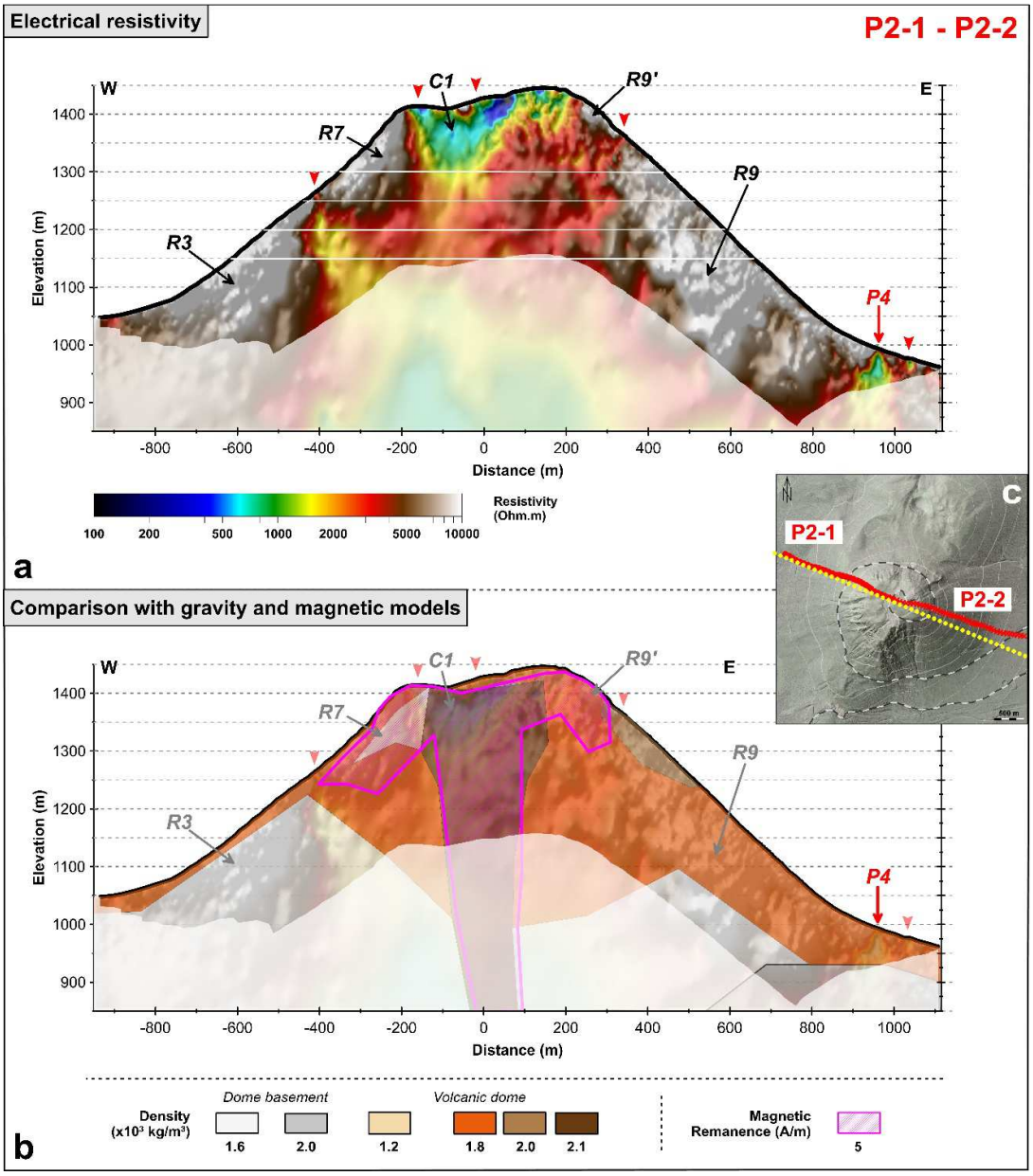

Fig. 9. (a) Vertical section extracted from the 3D inversion models of the entire Puy de Dôme edifice (Whole Dome Inversion – WDI) along the P2 ERT profile. (b) Comparison of the electrical results to the corresponding gravity and magnetic ones from (Portal et al., 2016). (c) Map of the location of the P2 line (red) and the corresponding section extracted from gravity and magnetism results (yellow dotted line). Opaque masks delineate the areas less constrained by the ERT measurements. Red arrows indicate local conductive patches associated to man-made structures (roads, paths, rails…). White lines (a only) refer to

horizontal slices on **Fig. 4**. Rn and Cn represent specific features related to resistive and conductive bodies, respectively.

5.3. The complex summit area

To analyze the sections in **Fig. 6**, we have to keep in mind that the thin (a few meters to a few tens of meters depth), highly resistive or conductive layers in this zone are strongly affected by various man-made structures and reworking.

The conductive zone *C1* occupies the central part of the summit area, but its shape, as well as the local variations in resistivity, are complex (**Fig. 5**). However, it exhibits clear characteristics:

- Considering its dimensions and its bulk resistivity, it constitutes a major structure;
- It has a maximum vertical extent of about 200 m;
- Its peripheral vertical limits are sharp;
- It may be composed of many sub-units separated by resistive structures (**Fig. 5** and **Fig. 6b, c** and **d**).

Therefore, *C1* could represent a single unit with resistive bodies embedded in it. Field observations show evidences of small fissures and fumarolic alteration in the upper part of the dome (Miallier et al., 2010; Portal et al., 2016). The hydrothermal activity is commonly observed on recent or active lava domes and associated to a conductive signature of the corresponding deposits (e.g. Bedrosian et al., 2007; Byrdina et al., 2017; Rosas-Carbajal et al., 2016; Zlotnicki et al., 1998). We therefore suggest that the *C1* anomaly is evidence of the presence of a former hydrothermal system in the upper part of the lava dome resulting into high fracturing combined to an important fumarolic alteration of the rocks. Nevertheless, the comparison between electrical models and results presented by Portal et al. (2016), show that this conductive body *C1* is not correlated to a specific density or magnetic pattern (**Fig. 8** and **Fig. 9**). Instead, they show the presence of dense, highly magnetized rocks in the central part of the dome, from the surface to possibly the base of the edifice. Because the data coverage in both gravity and magnetic data is high in the summit area, the shallowness of the top of the dense and magnetized bodies identified in the models is reliable. Moreover, fracturing and hydrothermal fluids circulations usually contribute to lower both the density and the magnetization of rocks (*e.g.* Bouligand et

al., 2014). To support resistivity, gravity and magnetic signatures, we propose the following hypothesis. The fumarolic alteration is concentrated along a network of small-cracks observed in the field as well as in the upper part of the deep-seated fractures network identified by Boudon et al. (2015), surrounding unaltered rocks (still dense and highly magnetized). In this case study, electrical results provide significant arguments on the level of rock alteration in the upper part of the dome.

6. Conclusion

The ERT imaging of Puy de Dôme volcano aims at investigating the overall inner structure of the dome as well as its summit area. The resulting datasets is large, and such a density of measurement is rare regarding the study of lava domes. Here we present the results of a 3D inversion of this electrical datasets as well as a confrontation with complementary geophysical results from Portal et al. (2016). Besides to confirm some elements of the synthetic model of the inner structure of the Puy de Dôme volcano proposed by Portal et al. (2016), the geological interpretation of the electrical results provide new details. The presence of massive units inside the collapse breccia are evidences of former trachytic intrusions, typical of an endogenous construction. Our results provide also precisions about the geometry of the deposits that covered the eastern flank, which definitively excludes a major flank collapse of the lava dome (Camus, 1975) and which allowed Boivin et al. (2017) to propose the presence of a welded cinder deposits issued from a second exogenous eruptive phase. Then, we highlight, for the first time, the boundaries of the former hydrothermal system of the Puy de Dôme volcano, focused in its summit part. The hydrothermal alteration also affects the feeding conduit of the lava dome, with an alteration that decreases with depth.

More generally, this study greatly contributes to our knowledge about the formation of volcanic domes although it appears difficult to draw a general model of such a complex phenomenon. It seems that the magmatic feeding is concentrated along an eruptive conduit. Its localization strongly depends of the volcano substratum and can evolve under the pressure of the accumulated volcanic deposits. The later constitute a substantial volume of the edifices as already observed during recent eruptions (*e.g.* Soufrière Hills volcano; Wadge et al., 2009).

393 This resistivity study of a complex volcanic edifice, as well as the associated
394 gravity and magnetic study (Portal et al., 2016) are important for evaluating the
395 capacity of geophysical methods to explore the interior of a volcano, and to define
396 the best strategy to implement for that purpose. For each method, and particularly for
397 resistivity, the necessity to have good data coverage is essential to be able to derive
398 3D models and characterize structures at different scales. Even with good coverage,
399 models uncertainties can make the geological identification of structures difficult,
400 especially with increasing depth. We thus prove that collecting data, which are
401 sensitive to different physical parameters (resistivity, density and magnetization),
402 constitutes a powerful means for discriminating the geology of structures that would
403 otherwise be impossible to distinguish with one parameter (*e.g.* the density allows us
404 to differentiate resistive porous unsaturated rocks from scoria deposits). This case
405 study of the Puy de Dôme is therefore important at two levels: for providing
406 information about the architecture of a complex lava dome, and for guiding the
407 strategy for studying other volcanic edifices.

408 ## Acknowledgements

409 The LIDAR data used in this study derive from a collective project driven by the
410 Centre Régional Auvergnat de l'Information Géographique (CRAIG), financially
411 supported by the Conseil Départemental du Puy-de-Dôme, the European Regional
412 Development Fund and the University of Clermont-Ferrand. Datasets are available
413 on request to the authors. We thank the students and permanent staff of the
414 Laboratoire Magmas et Volcans (LMV), the TOMUVOL collaboration and the
415 Observatoire de Physique du Globe de Clermont-Ferrand (OPGC) for participation
416 and logistics during field surveys. Finally, we thank the anonymous reviewer for
417 helping comments to improve this manuscript. This research was supported by the
418 French Government Laboratory of Excellence initiative n°ANR-10-LABX-0006, the
419 Région Auvergne and the European Regional Development Fund. This is Laboratory
420 of Excellence ClerVolc contribution number 308.

References

Barde-Cabusson, S., Gottsmann, J., Martí, J., Bolós, X., Camacho, A.G., Geyer, A., Planagumà, L., Ronchin, E., Sánchez, A., 2014. Structural control of monogenetic volcanism in the Garrotxa volcanic field (Northeastern Spain) from gravity and self-potential measurements. Bull. Volcanol. 76, 1–13. https://doi.org/10.1007/s00445-013-0788-0

Bedrosian, P.A., Unsworth, M.J., Johnston, M.J.S., 2007. Hydrothermal circulation at Mount St. Helens determined by self-potential measurements. J. Volcanol. Geotherm. Res. 160, 137–146. https://doi.org/10.1016/j.jvolgeores.2006.09.003

Boivin, P., Besson, J.-C., Briot, D., Deniel, C., Gourgaud, A., Labazuy, P., de Larouzière, F.-D., Langlois, E., Livet, M., Médard, E., Merciecca, C., Mergoil, J., Miallier, D., Morel, J.-M., Thouret, J.-C., Vernet, G., 2017. Volcanology of the Chaîne des Puys. Parc Nat. Régional la Chaîne des Puys (Ed.), Cart. Fasc. 6e édition 200pp.

Boudon, G., Balcone-Boissard, H., Villemant, B., Morgan, D.J., 2015. What factors control superficial lava dome explosivity? Sci. Rep. 5, 14551. https://doi.org/10.1038/srep14551

Bouligand, C., Glen, J.M.G., Blakely, R.J., 2014. Distribution of buried hydrothermal alteration deduced from high-resolution magnetic surveys in Yellowstone National Park. J. Geophys. Res. Solid Earth 119, 2595–2630. https://doi.org/10.1002/2013JB010802

Brothelande, E., Finizola, A., Peltier, A., Delcher, E., Komorowski, J.-C., Di Gangi, F., Borgogno, G., Passarella, M., Trovato, C., Legendre, Y., 2014. Fluid circulation pattern inside La Soufrière volcano (Guadeloupe) inferred from combined electrical resistivity tomography, self-potential, soil temperature and diffuse degassing measurements. J. Volcanol. Geotherm. Res. 288, 105–122. https://doi.org/10.1016/j.jvolgeores.2014.10.007

Brothelande, E., Lénat, J.-F., Normier, A., Bacri, C., Peltier, A., Paris, R., Kelfoun, K., Merle, O., Finizola, A., Garaebiti, E., 2015. Insights into the evolution of the Yenkahe resurgent dome (Siwi caldera, Tanna Island, Vanuatu) inferred from aerial high-resolution photogrammetry. J. Volcanol. Geotherm. Res. 299, 78. https://doi.org/10.1016/j.jvolgeores.2015.04.006

Byrdina, S., Friedel, S., Vandemeulebrouck, J., Budi-Santoso, A., Suhari, Suryanto, W., Rizal, M.H., Winata, E., Kusdaryanto, 2017. Geophysical image of the hydrothermal system of Merapi volcano. J. Volcanol. Geotherm. Res. 329, 30–40. https://doi.org/10.1016/J.JVOLGEORES.2016.11.011

Byrdina, S., Grandis, H., Sumintadireja, P., Caudron, C., Syahbana, D.K., Naffrechoux, E., Gunawan, H., Suantika, G., Vandemeulebrouck, J., 2018. Structure of the acid hydrothermal system of Papandayan volcano, Indonesia, investigated by geophysical methods. J. Volcanol. Geotherm. Res. 358, 77–86. https://doi.org/10.1016/J.JVOLGEORES.2018.06.008

Camus, G., 1975. La Chaîne des Puys - Étude structurale et volcanologique. Université de Clermont.

Chambers, J.E., Kuras, O., Meldrum, P.I., Ogilvy, R.D., Hollands, J., 2006. Electrical

resistivity tomography applied to geologic, hydrogeologic, and engineering investigations at a former waste-disposal site. Geophysics 71, B231–B239. https://doi.org/10.1190/1.2360184

Christiansen, R.L., Peterson, D.W., 1981. Chronology of the 1980 eruptive activity. US Geol. Surv. Prof. Pap 1250, 17–30.

Constable, S., Parker, R.L., 1987. Occam's inversion: A practial algorithm for generating smooth models from electromagnetic sounding data. Geophysics 52, 289–300.

Constable, S.C., Parker, R.L., Constable, C.G., 1987. Occam's inversion: A practical algorithm for generating smooth models from electromagnetic sounding data. Geophysics 52, 289–300. https://doi.org/10.1190/1.1442303

Dahlin, T., 1996. 2D resistivity surveying for environmental and engineering applications. First Break. https://doi.org/10.3997/1365-2397.1996014

Dahlin, T., Zhou, B., 2004. A numerical comparison of 2D resistivity imaging with 10 electrode arrays. Geophys. Prospect. 52, 379–398. https://doi.org/10.1111/j.1365-2478.2004.00423.x

de Groot-Hedlin, C., Constable, S.C., 1990. Occam's inversion to generate smooth, two-dimensional models from magnetotelluric data. Geophysics 55, 1613–1624. https://doi.org/10.1190/1.1442813

Fargier, Y., Antoine, R., Dore, L., Lopes, S.P., Fauchard, C., 2017. 3D assessment of an underground mine pillar by combination of photogrammetric and geoelectric methods. GEOPHYSICS 82, E143–E153. https://doi.org/10.1190/geo2016-0274.1

Fikos, I., Vargemezis, G., Zlotnicki, J., Puertollano, J.R., Alanis, P.B., Pigtain, R.C., Villacorte, E.U., Malipot, G.A., Sasai, Y., 2012. Electrical resistivity tomography study of Taal volcano hydrothermal system, Philippines. Bull. Volcanol. 74, 1821–1831. https://doi.org/10.1007/s00445-012-0638-5

Gresse, M., Vandemeulebrouck, J., Byrdina, S., Chiodini, G., Revil, A., Johnson, T.C., Ricci, T., Vilardo, G., Mangiacapra, A., Lebourg, T., Grangeon, J., Bascou, P., Metral, L., 2017. Three-Dimensional Electrical Resistivity Tomography of the Solfatara Crater (Italy): Implication for the Multiphase Flow Structure of the Shallow Hydrothermal System. J. Geophys. Res. Solid Earth 122, 8749–8768. https://doi.org/10.1002/2017JB014389

Günther, T., Rücker, C., Spitzer, K., 2006. Three-dimensional modelling and inversion of dc resistivity data incorporating topography - II. Inversion. Geophys. J. Int. 166, 506–517. https://doi.org/10.1111/j.1365-246X.2006.03011.x

Herd, R.A., Edmonds, M., Bass, V.A., 2005. Catastrophic lava dome failure at Soufrière Hills Volcano, Montserrat, 12–13 July 2003. J. Volcanol. Geotherm. Res. 148, 234–252. https://doi.org/10.1016/j.jvolgeores.2005.05.003

Lesparre, N., Grychtol, B., Gibert, D., Komorowski, J.-C., Adler, A., 2014. Cross-section electrical resistance tomography of La Soufriere of Guadeloupe lava dome. Geophys. J. Int. 197, 1516–1526. https://doi.org/10.1093/gji/ggu104

Levenberg, K., 1944. A method for the solution of certain problems in least squares.

508 Q. Appl. Math. 2, 164–168.

509 Lines, L.R., Treitel, S., 1984. A review of least-squares inversion and its application
510 to geophysical problems. Geophys. Prospect. 32, 159–186.
511 https://doi.org/10.1111/j.1365-2478.1984.tb00726.x

512 Loke, M.H., 2012. Tutorial: 2-D and 3-D electrical imaging surveys. Geotomo
513 Software, Malaysia.

514 Loke, M.H., Chambers, J.E., Rucker, D.F., Kuras, O., Wilkinson, P.B., 2013. Recent
515 developments in the direct-current geoelectrical imaging method. J. Appl.
516 Geophys. 95, 135–156. https://doi.org/10.1016/j.jappgeo.2013.02.017

517 Marescot, L., Rigobert, S., Palma Lopes, S., Lagabrielle, R., Chapellier, D., 2006. A
518 general approach for DC apparent resistivity evaluation on arbitrarily shaped 3D
519 structures. J. Appl. Geophys. 60, 55–67.
520 https://doi.org/10.1016/j.jappgeo.2005.12.003

521 Marquardt, D.W., 1963. An Algorithm for Least-Squares Estimation of Nonlinear
522 Parameters. J. Soc. Ind. Appl. Math. 11, 431–441.
523 https://doi.org/10.2307/2098941

524 Miallier, D., Boivin, P., Deniel, C., Gourgaud, A., Lanos, P., Sforna, M., Pilleyre, T.,
525 2010. The ultimate summit eruption of Puy de Dome volcano (Chaine des Puys,
526 French Massif Central) about 10,700 years ago. Comptes Rendus Geosci. 342,
527 847–854. https://doi.org/10.1016/j.crte.2010.09.004

528 Nicollin, F., Gibert, D., Beauducel, F., Boudon, G., Komorowski, J.-C., 2006.
529 Electrical tomography of La Soufrière of Guadeloupe Volcano: Field
530 experiments, 1D inversion and qualitative interpretation. Earth Planet. Sci. Lett.
531 244, 709–724. https://doi.org/10.1016/j.epsl.2006.02.020

532 Park, S.K., Van, G.P., 1991. Inversion of pole-pole data for 3-D resistivity structure
533 beneath arrays of electrodes. Geophysics 56, 951–960.
534 https://doi.org/10.1190/1.1443128

535 Portal, A., Gailler, L.-S., Labazuy, P., Lénat, J.-F., 2016. Geophysical imaging of the
536 inner structure of a lava dome and its environment through gravimetry and
537 magnetism. J. Volcanol. Geotherm. Res. 320, 88–99.
538 https://doi.org/10.1016/j.jvolgeores.2016.04.012

539 Revil, A., Johnson, T.C., Finizola, A., 2010. Three-dimensional resistivity tomography
540 of Vulcan's forge, Vulcano Island, southern Italy. Geophys. Res. Lett. 37, n/a-
541 n/a. https://doi.org/10.1029/2010GL043983

542 Robain, H., Bobachev, A., 2017. X2IPI□: user manual.

543 Rosas-Carbajal, M., Komorowski, J.-C., Nicollin, F., Gibert, D., 2016. Volcano
544 electrical tomography unveils edifice collapse hazard linked to hydrothermal
545 system structure and dynamics. Sci. Rep. 6, 29899.
546 https://doi.org/10.1038/srep29899

547 Rücker, C., Günther, T., Spitzer, K., 2006. Three-dimensional modelling and
548 inversion of dc resistivity data incorporating topography - I. Modelling. Geophys.
549 J. Int. 166, 495–505. https://doi.org/10.1111/j.1365-246X.2006.03010.x

550 Sato, H., Fujii, T., Nakada, S., 1992. Crumbling of dacite dome lava and generation

of pyroclastic flows at Unzen volcano. Nature 360, 664–666. https://doi.org/10.1038/360664a0

Soueid Ahmed, A., Revil, A., Byrdina, S., Coperey, A., Gailler, L., Grobbe, N., Viveiros, F., Silva, C., Jougnot, D., Ghorbani, A., Hogg, C., Kiyan, D., Rath, V., Heap, M.J., Grandis, H., Humaida, H., 2018. 3D electrical conductivity tomography of volcanoes. J. Volcanol. Geotherm. Res. 356, 243–263. https://doi.org/10.1016/j.jvolgeores.2018.03.017

Tarantola, A., 2005. Inverse Problem Theory, SIAM. ed.

Tikhonov, A., Arsenin, V., John, F., 1977. Solutions of ill-posed problems.

Wadge, G., Ryan, G.A., Calder, E.S., 2009. Clastic and core lava components of a silicic lava dome. Geology 37, 551–554. https://doi.org/10.1130/G25747A.1

Zlotnicki, J., Boudon, G., Viodé, J.P., Delarue, J.F., Mille, A., Bruère, F., 1998. Hydrothermal circulation beneath Mount Pelee inferred by self potential surveying. Structural and tectonic implications. J. Volcanol. Geotherm. Res. 84, 73–91. https://doi.org/10.1016/S0377-0273(98)00030-4